# Micromechanics-Based Elastoplastic Modeling of Functionally Graded Materials with Pairwise Particle Interactions

Qiliang Lin[1]; Liangliang Zhang[2]; Fangliang Chen, M.ASCE[3]; and Huiming Yin, M.ASCE[4]

**Abstract:** To understand the inelastic behavior of functionally graded materials (FGMs) containing aluminum particles in high-density polyethylene (HDPE), a micromechanics-based elastoplastic model was developed. It was assumed that the particle phase was in a linearly elastic state while the matrix phase could be in a plastic stage. The corresponding yield function for the matrix phase was investigated, where the pairwise interaction term and probabilistic spatial distribution of particles were used to accommodate the gradation of particle volume fraction. Accordingly, the overall elastoplastic stress-strain response was established through homogenization of the stress and strain fields. The modeling prediction was validated with experiments on a specific functionally graded material. Good agreement was observed between the model and experimental results. In this paper, the effect of various particle distribution functions and relative material stiffness on the elastoplastic behavior of FGMs is addressed and discussed. **DOI: 10.1061/(ASCE)EM.1943-7889.0001603.** 

**Author keywords:** Functionally graded panel; Elastoplastic behavior; Micromechanics-based model; Pairwise interaction; Homogenization.



## Introduction

Conventional laminated composite materials exhibit a discontinuity of material properties at the interface, which often results in stress concentration and various damage such as delamination, matrix cracking, and adhesive bond separation when subjected to environmental and mechanical loadings. However, as characterized by spatially graded reinforcement phases within the matrix phase in a continuous manner (Kumar and Dutta 1998), functionally graded materials (FGMs) possess continuously graded material properties and thus have many advantages over conventional laminated composite materials. For example, FGMs have potentially reduced in-plane and transverse through-the-thickness stresses (Birman and Byrd 2007), improved residual stress distribution (Miyamoto et al. 2013), enhanced thermal properties (Shen 2013), higher fracture toughness (Park et al. 2010), reduced stress intensity (Ayhan 2007, 2009), and so on. Because of these unique features, FGMs have gained much attention and have been widely used in many structural applications such as aerospace (Ganapathi et al. 2006), electrical engineering (Kargarnovin et al. 2007), biomedical engineering (Pompe et al. 2003), and nuclear and civil engineering (Yiatros et al. 2012). As examples, Yin et al. (2013) and Chen et al. (2016) showed that by developing FGMs constructed of coarse aluminum powder and high-density polyethylene (Al/HDPE) in a building-integrated photovoltaic thermal roofing panel, considerable efficiency in solar energy harvesting is achieved.

Due to the spatial variations in volume fractions of different phases, FGMs are essentially heterogeneous, which leads to limited analytical schemes to tackle the spatial variation in each phase. In past decades, micromechanics-based homogenization was considered an effective approach to analyze FGMs (Birman and Byrd 2007), where the materials were homogenized locally at the representative volume element (RVE) scale to achieve globally heterogeneous behavior at the macroscopic scale.

The equivalent inclusion method (EIM) (Eshelby 1957, 1959) was developed by Eshelby to account for inhomogeneity within an infinite matrix domain, such that the stiffness mismatch between particle and matrix could be represented by a so-called eigenstrain. With the introduction of eigenstrain, Eshelby (1957) developed the EIM to solve the elastic field of a single inhomogeneity within an infinite domain, in which the difference in material properties between particles and matrix was accommodated. This method was further modified and extended by Moschovidis and Mura (1975) to address the multiparticle problem and ellipsoidal shape. The EIM is a powerful tool because it gives detailed stress and strain fields for both particles and matrix. Thanks to the development of the ellipsoidal particle, it is capable of solving composites with different particle shapes. Ju and Chen (1994a, b) further developed the EIM and applied it to the elastic prediction of particle-reinforced metal matrix composites (PRMMCs) with spherical and spheroidal particles. As for the elastoplastic behavior of composites, based on previous work (Ju and Chen 1994a, b), effective PRMMC elastoplastic deformations and responses were estimated by virtue of the "effective yield criterion" (Ju and Chen 1994c), derived micromechanically by considering the effects of elastic spherical particles embedded in the elastoplastic matrix. Ju and Tseng (1996, 1997) extended this theory to particle-reinforced ductile matrix composites,

[1]Graduate Research Assistant, Dept. of Civil Engineering and Engineering Mechanics, Columbia Univ., 610 Seeley W. Mudd 500 West 120th St., New York, NY 10027. Email: ql2241@columbia.edu

[2]Postdoctoral Research Associate, Dept. of Civil Engineering and Engineering Mechanics, Columbia Univ., 610 Seeley W. Mudd 500 West 120th St., New York, NY 10027. Email: lz2612@columbia.edu

[3]Associate Research Scientist, Dept. of Civil Engineering and Engineering Mechanics, Columbia Univ., 610 Seeley W. Mudd 500 West 120th St., New York, NY 10027. Email: fangliangchen@yahoo.com

[4]Associate Professor, Dept. of Civil Engineering and Engineering Mechanics, Columbia Univ., 610 Seeley W. Mudd 500 West 120th St., New York, NY 10027 (corresponding author). Email: yin@civil.columbia.edu

Note. This manuscript was submitted on July 3, 2018; approved on October 18, 2018; published online on March 15, 2019. Discussion period open until August 15, 2019; separate discussions must be submitted for individual papers. This paper is part of the ***Journal of Engineering Mechanics***, © ASCE, ISSN 0733-9399.

and presented an analytical expression of bulk and shear moduli for two-phase composites that accounted for pairwise spherical particle interaction. The overall elastoplastic stress-strain response of randomly located, aligned/random-oriented particles merged into metal matrix composites was studied by virtue of previous work (Sun and Ju 2001, 2004).

Other inelastic problems have been widely studied for different types of composites. A novel self-consistent modeling based on the translated field method was developed by Mareau and Berbenni (2015) to solve the elastoviscoplastic problems of fiber-reinforced composites and polycrystalline materials. Misra and Poorsolhjouy (2015) proposed a granular micromechanics model using grain-scale force-displacement relationships to deal with the damage-plasticity problems of cementitious materials with thermal effect. Misra and Yang (2010) extended this approach for cohesive materials as well as rate-dependent materials (Misra and Singh 2013). Marfia and Sacco (2018) presented a multiscale technique for studying the nonlinear behavior of metal matrix composites, where piecewise uniform transformation field analysis homogenization for the microscale and a unit cell containing all properties of the heterogeneous materials for the macroscale were considered separated.

The majority of studies just mentioned focused mainly on homogeneous composites with uniform particle distribution (i.e. material gradation being zero). When FGMs with polymeric matrices are subjected to externally applied mechanical or thermal loadings, plastic deformation commonly develops. In this respect, elastoplastic analysis of FGMs is needed.

By comparison with the micromechanical model of FGMs, Gasik (1998) provided the Gasik-Ueda model to characterize the elastoplastic properties of FGM which worked for dilute distribution of particles in a uniform matrix without considering the interaction of particles. Following the micromechanics scheme, Yin et al. (2004) proposed an elastic algorithm that contained the coupling effect of neighboring layers and the pairwise interaction effect between particles to accommodate the grading nature of FGMs, which was extended to the thermomechanical (Yin et al. 2008) and interfacial debonding (Paulino et al. 2006) behavior of FGMs. However, to the best of the authors' knowledge, an elastoplastic algorithm that micromechanically considers particle interaction for FGMs has yet to be found in the literature.

In this study, a micromechanics-based elastoplastic model that considers pairwise particle interaction in FGMs was developed. A two-phase FGM was studied, with the assumption that plastic deformation occurs only in the matrix phase. In this paper, a brief introduction of micromechanical formulation is given, with its application to the elastic analysis of FGMs. The corresponding plastic algorithm is then discussed, where the ensemble average yield function is introduced with the corresponding stress norm. Next, validation of the proposed method through uniaxial compression testing of a specific FGM, where good agreement was reached, is taken up, followed by an explanation of the parametric studies conducted, focusing on the effects of various particle distribution functions and varying relative material stiffness. Finally, some conclusions are provided.

## Micromechanical Formulation

### Micromechanics-Based Model with Equivalent Inclusion Method

The elastic behavior of FGMs is discussed in detail by Yin et al (2004), through the equivalent inclusion method (EIM) originated by Eshelby (1957). A brief review is given in this section to introduce background and to formulate a complete elastoplastic algorithm. In the EIM, the strain field of one particle embedded in an infinite domain is decomposed into a far-field strain $\boldsymbol{\varepsilon}^0$ and a disturbed strain $\boldsymbol{\varepsilon}'$ (Yin and Zhao 2016)

$$\boldsymbol{\varepsilon} = \boldsymbol{\varepsilon}^0 + \boldsymbol{\varepsilon}' \tag{1}$$

where the disturbed strain of $\boldsymbol{\varepsilon}'$ due to elastic mismatch between the particles and the matrix is computed through the modified Green's function $\boldsymbol{G}(\boldsymbol{x}, \boldsymbol{x}')$

$$\boldsymbol{\varepsilon}' = -\int_{\boldsymbol{\Omega}} \boldsymbol{G}(\boldsymbol{x}, \boldsymbol{x}') \cdot \boldsymbol{C}_0 : \boldsymbol{\varepsilon}^*(\boldsymbol{x}') d\boldsymbol{x}' \tag{2}$$

where $\boldsymbol{\Omega}$ = particle domain; $\boldsymbol{C}_0$ = matrix elastic stiffness tensor ($\boldsymbol{C}_1$ = particle elastic stiffness tensor); and $\boldsymbol{\varepsilon}^*$ = eigenstrain to simulate the material mismatch under the far-field load.

For a single particle embedded in the infinite domain, the stress equivalent condition in the spherical particle domain is used to compute the eigenstrain under the stiffness mismatch

$$\boldsymbol{C}_1 : (\boldsymbol{\varepsilon}^0 + \boldsymbol{\varepsilon}') = \boldsymbol{C}_0 : (\boldsymbol{\varepsilon}^0 + \boldsymbol{\varepsilon}' - \boldsymbol{\varepsilon}^*) \tag{3}$$

after which the eigenstrain is related through the disturbed strain $\boldsymbol{\varepsilon}'$ and computed as

$$\boldsymbol{\varepsilon}^* = \boldsymbol{C}_0^{-1} \cdot (\boldsymbol{D}^{\Omega} - \Delta \boldsymbol{C}^{-1})^{-1} : \boldsymbol{\varepsilon}^0 \tag{4}$$

where $\Delta \boldsymbol{C} = \boldsymbol{C}_1 - \boldsymbol{C}_0$; and $\boldsymbol{D}^{\Omega}$ = integration of the modified Green's function within the particle domain and can be found in (Yin and Zhao 2016).

Combining Eqs. (1), (2), and (4), the strain field within the spherical particle domain is computed as

$$\bar{\boldsymbol{\varepsilon}} = (\boldsymbol{I} - \boldsymbol{D}^{\Omega} \cdot \Delta \boldsymbol{C})^{-1} : \boldsymbol{\varepsilon}^0 \tag{5}$$

The EIM scheme is extended to two spherical particles, and the averaged strain field within one of the two particles' domains is derived as

$$\bar{\bar{\boldsymbol{\varepsilon}}} = \frac{1}{V_{\Omega}} \int_{\Omega} \boldsymbol{\varepsilon} d\boldsymbol{\Omega} = (\boldsymbol{I} - \boldsymbol{D}^{\Omega} \cdot \Delta \boldsymbol{C} - \boldsymbol{D} \cdot \Delta \boldsymbol{C})^{-1} : \boldsymbol{\varepsilon}^0 + O(\tilde{\rho}^8) \tag{6}$$

where $\tilde{\rho} = a/b$ and $V_{\boldsymbol{\Omega}} = 4\pi a^3/3$; $a$ = particle radius; $b$ = center-to-center distance between the two particles centered at $\boldsymbol{x}_1$ and $\boldsymbol{x}_2$; $\boldsymbol{D}$ = integration of the modified Green's function inside the matrix domain, where the other particle is located. Precision can reach the order of $O(\tilde{\rho}^8)$, where $\tilde{\rho}$ is not higher than 0.5.

Eq. (6) represents the volume average strain inside one of the two particles, under the influence of the other. Subtracting Eq. (5) from Eq. (6), the average influence of the second particle on first particle's domain is given as

$$\boldsymbol{d}(\boldsymbol{x}_1, \boldsymbol{x}_2) = \bar{\bar{\boldsymbol{\varepsilon}}} - \bar{\boldsymbol{\varepsilon}} = \Delta \boldsymbol{C}^{-1} \cdot \boldsymbol{L}(\boldsymbol{x}_1, \boldsymbol{x}_2) : \boldsymbol{\varepsilon}^0 \tag{7}$$

where the pairwise interaction tensor $\boldsymbol{L}(\boldsymbol{x}_1, \boldsymbol{x}_2)$ is

$$\boldsymbol{L}(\boldsymbol{x}_1, \boldsymbol{x}_2) = ([\Delta \boldsymbol{C}^{-1} - \boldsymbol{D}^{\Omega} - \boldsymbol{D}]^{-1} - [\Delta \boldsymbol{C}^{-1} - \boldsymbol{D}^{\Omega}]^{-1}) + O(\tilde{\rho}^8) \tag{8}$$

Eq. (7) can be extended to represent the influence of multiple particles $P_i (i = 2, 3, \ldots)$ on a particle $P_1(\boldsymbol{x}_1)$ to the pairwise level, such that for a given particle configuration $\mathcal{G}$ with $N$ particles, the average strain inside the first particle domain is given with the pairwise particle influence as

$$\bar{\bar{\boldsymbol{\varepsilon}}}(\boldsymbol{x}_1) = (\boldsymbol{I} - \boldsymbol{D}^{\Omega} \cdot \boldsymbol{\Delta C})^{-1} : \boldsymbol{\varepsilon}^0 + \sum_{i=2}^{N} \boldsymbol{d}(\boldsymbol{x}_1, \boldsymbol{x}_i) \tag{9}$$

### Elastic Analysis of Functionally Graded Materials

The microstructure of a typical FGM is shown in Fig. 1. The gradation direction is assumed to be along the $X_3(x_3)$ axis. A microscopic RVE with coordinate $\boldsymbol{x}$ is centered at a macroscopic point $\boldsymbol{X}$. Without loss of generality, it is assumed that a particle $P_1$ exists at the center $\boldsymbol{x} = \boldsymbol{0}$ of the microscopic RVE. With the help of Eq. (9), the averaged strain inside the domain of particle $P_1$ is given as

$$\langle \boldsymbol{\varepsilon} \rangle^{P_1} = (\boldsymbol{I} - \boldsymbol{D}^{\Omega} \cdot \boldsymbol{\Delta C})^{-1} : \boldsymbol{\varepsilon}^0(P_1) + \sum_{i=2}^{\infty} \boldsymbol{\Delta C}^{-1} \cdot \boldsymbol{L}(P_1, P_i) : \boldsymbol{\varepsilon}^0(P_i) \tag{10}$$

where $\boldsymbol{\varepsilon}^0(P_i)$ = prescribed far-field strain at the same height as that of the corresponding particle, which varies along the microscopic field with particle volume fraction, such that Eq. (10) can be further written as

$$\langle \boldsymbol{\varepsilon} \rangle(\boldsymbol{0}) = (\boldsymbol{I} - \boldsymbol{D}^{\Omega} \cdot \boldsymbol{\Delta C})^{-1} : \boldsymbol{\varepsilon}^0(\boldsymbol{0}) + \sum_{i=1}^{\infty} \boldsymbol{\Delta C}^{-1} \cdot \boldsymbol{L}(\boldsymbol{0}, \boldsymbol{x}^i) : \boldsymbol{\varepsilon}^0(x_3^i) \tag{11}$$

where the prescribed far-field strain $\boldsymbol{\varepsilon}^0(x_3^i)$ is related to the far-field strain at the center of the RVE $\boldsymbol{\varepsilon}^0(\boldsymbol{0})$ by the Taylor expansion to the first order,

$$\boldsymbol{\varepsilon}^0(x_3^i) \cong \boldsymbol{\varepsilon}^0(\boldsymbol{0}) + \boldsymbol{\varepsilon}^0_{,3}(\boldsymbol{0})(\boldsymbol{x}^i - \boldsymbol{0}) = \boldsymbol{\varepsilon}^0(\boldsymbol{0}) + \boldsymbol{\varepsilon}^0_{,3}(\boldsymbol{0}) x_3 \tag{12}$$

Since all particles are statistically distributed microscopically in a random way, a probability function $P(\boldsymbol{x}|\boldsymbol{0})$ is introduced to statistically represent the probability of a particle centered at $\boldsymbol{x}$ when another particle is centered at $\boldsymbol{0}$, which converts the summation of Eq. (11) into integration

$$\begin{aligned} \langle \boldsymbol{d} \rangle(\boldsymbol{0}) &= \sum_{i=1}^{\infty} \boldsymbol{\Delta C}^{-1} \cdot \boldsymbol{L}(\boldsymbol{0}, \boldsymbol{x}^i) : \boldsymbol{\varepsilon}^0 x_3^i \\ &= \int_D P(\boldsymbol{x}|\boldsymbol{0}) \boldsymbol{\Delta C}^{-1} \cdot \boldsymbol{L}(\boldsymbol{0}, \boldsymbol{x}^i) : \boldsymbol{\varepsilon}^0(x_3^i) d\boldsymbol{x} \end{aligned} \tag{13}$$

The particle density function $P(\boldsymbol{x}|\boldsymbol{0})$ is also expanded with Taylor expansion to the first order to accommodate the gradation of particle distribution

$$P(\boldsymbol{x}|\boldsymbol{0}) = \frac{3}{4\pi a^3} [\phi(X_3) + e^{-\frac{\boldsymbol{x}}{\delta}} \phi_{,3}(X_3) \cdot x_3] \tag{14}$$

where $\delta$ = parameter to control the attenuation rate such that the probability density function remains within a reasonable range inside the RVE.

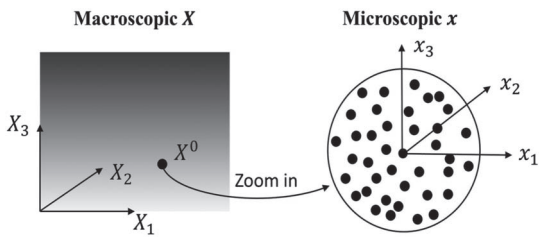


**Fig. 1.** Micromechanics-based model of an FGM cross the macroscopic and microscopic scales.

Eqs. (12)–(14) are plugged into Eq. (11) for the explicit relation between particle strain and prescribed far-field strain as

$$\begin{aligned} \langle \boldsymbol{\varepsilon} \rangle(X_3) = (\boldsymbol{I} - \boldsymbol{D}^{\Omega} \cdot \boldsymbol{\Delta C})^{-1} : \boldsymbol{\varepsilon}^0(X_3) + \phi \boldsymbol{\Delta C}^{-1} \cdot \boldsymbol{\mathcal{D}} : \boldsymbol{\varepsilon}^0(X_3) \\ + \phi_{,3} \boldsymbol{\Delta C}^{-1} \cdot \boldsymbol{\mathcal{F}} : \boldsymbol{\varepsilon}^0_{,3}(X_3) \end{aligned} \tag{15}$$

Tensor $\boldsymbol{\mathcal{D}}$ addresses the pairwise interaction between particles, while tensor $\boldsymbol{\mathcal{F}}$ accounts for the coupling of layers along the gradation direction. Eq. (15) relates the ensemble average particle strain $\langle \boldsymbol{\varepsilon} \rangle(X_3)$ to its corresponding prescribed far-field strain $\boldsymbol{\varepsilon}^0(X_3)$, which is macroscopically equivalent to the matrix strain. The overall macroscopic stress $\bar{\boldsymbol{\sigma}}$ can be derived as the volume average of the particle and matrix stress, so

$$\bar{\boldsymbol{\sigma}} = \phi(X_3) \boldsymbol{C}_1 : \langle \boldsymbol{\varepsilon} \rangle(X_3) + [1 - \phi(X_3)] \boldsymbol{C}_0 : \langle \boldsymbol{\varepsilon} \rangle^0(X_3) \tag{16}$$

Given $\bar{\boldsymbol{\sigma}}$, Eqs. (15) and (16) formulate an ordinary differential equation that can be solved by the backward Euler's method, such that the elastic behavior of FGMs considering pairwise particle interaction is well defined.

### Effective Plastic Behavior of FGMs

In the plastic analysis of two-phase FGMs, it is assumed that plasticity only occurs in the matrix phase while the particles stay in the elastic phase. The von Mises associated yield rule with isotropic hardening is considered (Simo and Hughes 2006) as

$$F(\boldsymbol{\sigma}, e^p) = \sqrt{H} - \sqrt{\frac{2}{3}} K(e^p) \tag{17}$$

For an isotropic homogeneous material, the stress norm takes the form $H = \boldsymbol{\sigma} : \boldsymbol{I_d} : \boldsymbol{\sigma}$, and the isotropic hardening function takes the form $K(e^p) = \sigma_Y + h(e^p)^q$, where $\sigma_Y$ is the yield stress, $h$ and $q$ are the hardening parameters, and $e^p$ is the effective plastic strain. However, such stress norm definition is suitable for isotropic homogeneous material and can only be applied at the microscopic scale. An ensemble average stress norm and the corresponding effective yield function that defines the macroscopic behavior is needed. Following Ju and Chen's framework (Ju and Chen 1994c), the volume average stress norm is defined as:

$$\sqrt{\langle H \rangle} = (1 - \phi) \sqrt{\langle H \rangle_m} \tag{18}$$

where $\langle H \rangle_m$ stands for the ensemble average stress norm of matrix phase. Hardening occurs only in matrix phase, with no contribution from the particle phase. Therefore, $e^p$ in Eq. (18) is replaced by the matrix effective plastic strain $e^p_m$. The ensemble average yield function for two-phase FGM is written as

$$\bar{F}(\sigma, e^p_m) = (1 - \phi) \sqrt{\langle H \rangle_m} - \sqrt{\frac{2}{3}} K(e^p_m) \tag{19}$$

Given a particle configuration $\boldsymbol{\mathcal{G}}$, the ensemble average stress norm of matrix is defined as

$$\langle H \rangle_m(x) = H^0 + \int_{\boldsymbol{\mathcal{G}}} \{H(\boldsymbol{x}|\boldsymbol{\mathcal{G}}) - H^0\} P(\boldsymbol{\mathcal{G}}) d\boldsymbol{\mathcal{G}} \tag{20}$$

where $H^0 = \boldsymbol{\sigma}^0 : \boldsymbol{I_d} : \boldsymbol{\sigma}^0$ = stress norm of the prescribed far-field stress $\boldsymbol{\sigma}^0$. Since the evaluation based on the real particle configuration $\boldsymbol{\mathcal{G}}$ is impossible, the higher-order effect of particle influence in Eq. (20) is neglected, leaving only the first-order influence of the particle on

the matrix, creating a simplified ensemble average stress norm of the matrix phase

$$\langle H\rangle_m(\boldsymbol{x}) = H^0 + \int_{|\boldsymbol{x}-\boldsymbol{x}_1|>a} \{H(\boldsymbol{x}|\boldsymbol{x}_1) - H^0\} P(\boldsymbol{x}_1) d\boldsymbol{x}_1 \quad (21)$$

where $P(\boldsymbol{x}_1)$ = probability density function and has the form of Eq. (14).

With the aid of Eqs. (1), (2), and (4), the matrix stress is evaluated as

$$\boldsymbol{\sigma} = \boldsymbol{\sigma}^0 + \boldsymbol{\sigma}' = (\boldsymbol{I} + \boldsymbol{A}):\boldsymbol{\sigma}^0 \quad (22)$$

where $\boldsymbol{A} = -\boldsymbol{D}:(\boldsymbol{D}^\Omega - \Delta\boldsymbol{C}^{-1})^{-1}$.

Substituting Eq. (22) into Eq. (21) yields the explicit form of the ensemble average stress norm of the matrix as follows:

$$\begin{aligned}\langle H\rangle_m(\boldsymbol{x}) &= H^0 + \int_{|\boldsymbol{x}-\boldsymbol{x}_1|>a} \{\boldsymbol{A}^{\mathrm{T}}:\boldsymbol{I_d}:\boldsymbol{A} + \boldsymbol{A}^{\mathrm{T}}:\boldsymbol{I_d} + \boldsymbol{I_d}:\boldsymbol{A}\} P(\boldsymbol{x}_1) d\boldsymbol{x}_1 \\ &= \boldsymbol{\sigma}^0:\boldsymbol{T}^0:\boldsymbol{\sigma}^0 \end{aligned} \quad (23)$$

where $\boldsymbol{A}^{\mathrm{T}}$ is the transpose of $\boldsymbol{A}$.

Here, the components of the fourth-rank tensor $\boldsymbol{T}^0$ are given by

$$T^0_{ijkl} = T^0_1\delta_{ij}\delta_{kl} + T^0_2(\delta_{ik}\delta_{jl} + \delta_{il}\delta_{jk}) \quad (24)$$

with

$$3T^0_1 + 2T^0_2 = \frac{(3\alpha + 2\beta)^2(1-2v_0)^2\phi}{18(1-v_0)^2\mu_0^2} \quad (25)$$

$$T^0_2 = \frac{1}{2} + \frac{\phi(23 - 50v_0 + 35v_0^2)\beta^2}{225(1-v_0)^2\mu_0^2} \quad (26)$$

where $\mu_0$ and $\nu_0$ are the shear modulus and Poisson ratio of matrix phase, correspondingly, and the $\alpha$ and $\beta$ are defined as: $\alpha = \frac{-\gamma}{3\gamma+2\eta}$, $\beta = \frac{1}{4\eta}$ with $\gamma = \frac{1}{30\mu_0(1-\nu_0)} - (\frac{1}{9\Delta k} - \frac{1}{6\Delta\mu})$, $\eta = \frac{5\nu_0-4}{30\mu_0(1-\nu_0)} - \frac{1}{4\Delta\mu}$.

Eq. (24) gives the stress norm that accounts for the first-order particle–matrix influence. It assumes dilute particle configuration so that the disturbed strain field from each particle can be linearly superposed. Pairwise particle interaction is considered when the volume fraction is high. Eqs. (15) and (16) give the relation between the ensemble average stress and the far-field stress $\boldsymbol{\sigma}^0$ as

$$\boldsymbol{\sigma}^0 = \boldsymbol{P}:\bar{\boldsymbol{\sigma}} \quad (27)$$

Eq. (27) holds for each individual layer $(\boldsymbol{\sigma}^0)^i = \boldsymbol{P}^i:(\bar{\boldsymbol{\sigma}})^i$; however, the derivative of the far-field strain $\boldsymbol{\varepsilon}^0_{,3}$ makes the fourth-rank tensor $\boldsymbol{P}$ implicit, to be solved numerically by the backward Euler's method in each layer in the gradation direction as follows:

$$(\bar{\boldsymbol{\sigma}})^i = \boldsymbol{H}:(\boldsymbol{\sigma}^0)^i + \boldsymbol{Q}:(\boldsymbol{\sigma}^0)^{i-1} \quad (28)$$

where $(\cdot)^i$ = quantity in the $i$th layer along the thickness; and

$$\begin{aligned}\boldsymbol{H} = \{&\phi\boldsymbol{C}_1 \cdot [(\boldsymbol{I} - \boldsymbol{D}^\Omega \cdot \Delta\boldsymbol{C})^{-1} + \phi\Delta\boldsymbol{C}^{-1} \cdot \boldsymbol{\mathcal{D}}] \cdot \boldsymbol{C}_0^{-1} \\ &+ (1-\phi)\boldsymbol{I}\} - \boldsymbol{Q}\end{aligned} \quad (29)$$

$$\boldsymbol{Q} = -\frac{N}{t}\phi_{,3}\phi\boldsymbol{C}_1 \cdot \Delta\boldsymbol{C}^{-1} \cdot \boldsymbol{\mathcal{F}} \cdot \boldsymbol{C}_0^{-1} \quad (30)$$

where $t$ = thickness; and $N$ = number of layers along the gradation. Based on the equilibrium, the ensemble average stresses are the same in each layer $(\bar{\boldsymbol{\sigma}})^i = (\bar{\boldsymbol{\sigma}})^j$. Plugging Eq. (27) into Eq. (28) gives

$$\boldsymbol{I} = \boldsymbol{H}:\boldsymbol{P}^i + \boldsymbol{Q}:\boldsymbol{P}^{i-1} \quad (31)$$

The boundary at $i = 1$ corresponds to the 100% matrix material, such that an explicit equation can be formulated by Eqs. (16) and (17) to calculate $\boldsymbol{P}^0$. For FGMs where the particle volume fraction does not start from 0%, the boundary condition can be formulated by dropping the $\boldsymbol{Q}$ term in Eq. (29). With the help of Eq. (27), the stress norm is written in terms of ensemble average stress as

$$\langle\boldsymbol{H}\rangle^i_{\boldsymbol{m}}(\boldsymbol{x}) = \bar{\boldsymbol{\sigma}}:\bar{\boldsymbol{T}}^i:\bar{\boldsymbol{\sigma}} \quad (32)$$

where the fourth-order tensor $\bar{\boldsymbol{T}}^i$ is defined as

$$\bar{\boldsymbol{T}}^i = \boldsymbol{P}^i:\boldsymbol{T}^0:\boldsymbol{P}^i \quad (33)$$

Therefore, the yield function for FGMs becomes

$$\bar{F}^i(\bar{\boldsymbol{\sigma}}, e^p_m) = (1-\phi)\sqrt{\bar{\boldsymbol{\sigma}}:\bar{\boldsymbol{T}}^i:\bar{\boldsymbol{\sigma}}} - [\sigma_Y + h(e^{pi}_m)^q] \quad (34)$$

Following the associative flow rule, the macroscopic plastic strain in each layer is determined by

$$\dot{\bar{\boldsymbol{\varepsilon}}}^p = \dot{\lambda}\frac{\partial\bar{F}}{\partial\bar{\boldsymbol{\sigma}}} = \dot{\lambda}(1-\phi)\frac{\bar{\boldsymbol{T}}:\bar{\boldsymbol{\sigma}}}{\sqrt{\bar{\boldsymbol{\sigma}}:\bar{\boldsymbol{T}}:\bar{\boldsymbol{\sigma}}}} \quad (35)$$

Accordingly, the effective plastic strain for the matrix is

$$\dot{e}^p_m = \frac{\dot{e}^p}{1-\phi} = \frac{1}{1-\phi}\sqrt{\frac{2}{3}\dot{\bar{\boldsymbol{\varepsilon}}}^p:\dot{\bar{\boldsymbol{\varepsilon}}}^p} \quad (36)$$

The macroscopic total strain is the volumetric average of the particle and the matrix

$$\langle\boldsymbol{\varepsilon}\rangle = (1-\phi)\boldsymbol{\varepsilon}_m + \phi\boldsymbol{\varepsilon}_p \quad (37)$$

where the matrix strain is the combination of its elastic and plastic part $\boldsymbol{\varepsilon}_m = \boldsymbol{\varepsilon}^e_m + \boldsymbol{\varepsilon}^p_m$, while the particle total strain contains only the elastic part $\boldsymbol{\varepsilon}_p = \boldsymbol{\varepsilon}^e_p$. The elastic part, $\boldsymbol{\varepsilon}^e_m$ and $\boldsymbol{\varepsilon}^e_p$, is determined through the elastic algorithm described by Eqs. (15) and (16)while the plastic part, $\boldsymbol{\varepsilon}^p_m$, is defined by Eqs. (34)–(36). If the macroscopic ensemble average stress $\bar{\boldsymbol{\sigma}}$ is known, the consistency condition requires the yield function [Eq. (28)] to be smaller than or equal to zero, which determines the effective plastic strain directly. In case of strain-driven plasticity, the return mapping algorithm is applied to determine $\dot{\lambda}$ from the consistency condition and perform the stress update.

## Experimental Validation

Although experimental data for plastic loading of FGMs are not found in the literature, the plastic behavior of particle-reinforced metal matrix composites (PRMMCs) is well documented, where the reinforcing particles are assumed to be uniformly distributed in the metal matrix to exhibit overall homogeneous mechanical behavior. The proposed model is downgraded for the elastoplastic behavior prediction of PRMMC for comparison with Ju and Chen's (1994c) model as well as experiments conducted by Yang et al. (1991). Good agreement has been achieved, and the detailed discussion can be found in Zhang et al. (submitted, *Int. J. Plast*, Elsevier, Amsterdam, Netherlands).

Elastoplastic tests of a specific FGM developed from the authors' recent research were conducted and compared with theoretical predictions. The FGM was made from coarse aluminum powder (Al-111) and high-density polyethylene (HDPE) via the vibration method. Al-111 was chosen to mix with the finer HDPE powder. The desired gradation of the Al/HDPE FGM in terms of volume

**Table 1.** FGM sample dimensions and weights

| Sample | H [mm (in.)] | W [mm (in.)] | D [mm (in.)] | Weight (g) |
|---|---|---|---|---|
| 1 | 13.39 (0.5273) | 13.27 (0.5223) | 14.24 (0.5605) | 3.40 |
| 2 | 13.52 (0.5324) | 13.62 (0.5361) | 13.27 (0.5223) | 3.30 |
| 3 | 13.20 (0.5198) | 13.18 (0.5188) | 13.35 (0.5254) | 3.16 |
| 4 | 13.63 (0.5366) | 13.75 (0.5414) | 13.61 (0.5359) | 3.43 |
| Average | 13.44 (0.5290) | 13.45 (0.5296) | 13.61 (0.5360) | 3.32 |

fraction of aluminum to the FGM was 0%–50% across its thickness. Aiming at this gradation, a mixing design with an appropriate Al-to-HDPE volume ratio of 1:3 was applied and the ethanol added was determined by an ethanol–to–mixed powder weight ratio of 28%. Details on the mix design and fabrication processes are provided in Yang et al. (1991).

The uniaxial elastoplastic compression test was conducted with pure HDPE samples to obtain the elastoplastic material properties from the loading curve such that $E = 550$ MPa, $v = 0.3$, $\sigma_Y = 17.6$ MPa, $h = 67.5$ MPa, and $q = 0.5444$. Four cubic FGM samples were cut from an FGM plate for the uniaxial compression test (dimension and weight information is provided in Table 1). The samples were uniaxially compressed with the Instron 5984 34-k Universal Testing Machine at the Carleton Laboratory of Columbia University. The samples were loaded at 0.51 mm/min (0.02 in./min) until 1.52-mm (0.06-in.) total deformation was reached, where the approximate total deformation was about 10%.

Since authentic particle distribution along thickness is hard to obtain through direct measurement, an innovative image-based method was proposed to statistically retrieve it so that an accurate elastoplastic prediction could be achieved to compare with the experiment. The authors' particle distribution along the FGM thickness is determined through image analysis as $\phi(x) = -0.5169x^2 + 0.8130x$, where $x$ is the relative location along the gradation direction. The elastoplastic loading curves for all four FGM samples were recorded and plotted in Fig. 2, where the error bar represents the maximum deviation of all four samples. Predicted elastoplastic behavior under authentic particle volume fraction distribution is plotted with solid line.

Fig. 2 shows that experimental data from the four FGM samples exhibited similar elastoplastic behavior with a narrow deviation

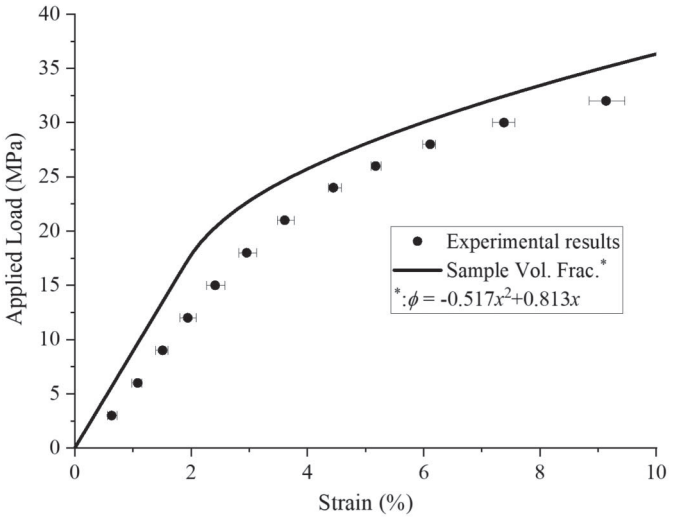


**Fig. 2.** FGM elastoplastic behavior: experimental and predicted.

over the entire loading process. The theoretical elastoplastic prediction based on authentic particle volume fraction distribution slightly underestimated overall deformation, but captured the trend of behavior very well. The prediction mismatch was mostly in the elastic stage and became less obvious during the plastic stage. The underestimation of deformation may have resulted from the effect of debonding and the imperfect interface between the aluminum particles and the HDPE matrix and from the potential air voids inside the samples, which were neglected in the theoretical derivation. The proposed algorithm was developed based on the assumption of spherical particles, which may also have contributed to the imperfect match. Overall, the proposed elastoplastic algorithm captured the real elastoplastic behavior of FGMs very well and can be used for further investigation and industry prediction.

It is also worthwhile to point out that HDPE is a highly viscous and thermoplastic material, such that time and temperature have a significant influence on its overall mechanical behavior. Rate-dependent plasticity can happen if loads are applied over long time periods. In the current study, thermo and viscous effects were neglected thanks to short loading times in the uniaxial loading test. To fully understand the elastoplastic behavior of HDPE-based FGMs, more investigation on thermal and viscous effects will be carried out in the future.

## Parametric Studies

From our previous preliminary studies, it was concluded that when the overall particle volume fraction is fixed, the effective Young's modulus is slightly dependent on the distribution function; plastic behavior is strongly affected by both overall particle volume fraction and the type of particle distribution. However, relevant studies have been limited to quadratic and linear distribution with similar trends, and their conclusions no longer hold for extreme particle configurations, such as overly sedimented (delaminated) composites and insufficiently sedimented homogeneous FGMs, which are common in the both laboratory testing and industry manufacturing.

Besides volume fraction and particle distribution, the relative mechanical properties of particles over matrix significantly influence the elastoplastic behavior of FGMs. In this section, these are further investigated to clarify the effective elastoplastic behaviors of FGMs. The mechanical parameters used in this study were set as $E_0 = 550$ MPa, $v_0 = 0.3$, $\sigma_Y = 17.6$ MPa, $h = 67.5$ MPa, $q = 0.5444$ for the HDPE matrix and $E_1 = 70$ GPa, $v_1 = 0.33$ for the Al particles. The effective Young's modulus $E_e$, the overall offset yield stress $\sigma_{0.2}$, and the corresponding total strain $\varepsilon_{0.2}$ were used for comparison.

### *Effect of Different Volume Fractions*

Fig. 3 shows the elastoplastic predictions for FGMs under different particle distributions, which include uniform, root, quadratic, linear, and sigmoid. The overall particle volume fractions are the same as those of the samples in the experiment: 23.42%. The effective Young's modulus $E_e$, the offset yield stress $\sigma_{0.2}$, and the corresponding total strain $\varepsilon_{0.2}$ are provided in Table 2 for comparison. The particle distributions in this study were versatile, where extreme cases such as homogeneously mixed and overly sedimented FGMs were considered. The overall composite stiffness reached its strongest under uniform particle distribution and gradually weakened with increasing particle distribution order. The overly sedimented FGM, represented by the sigmoid function, showed the weakest material stiffness (Fig. 3). The effective Young's modulus

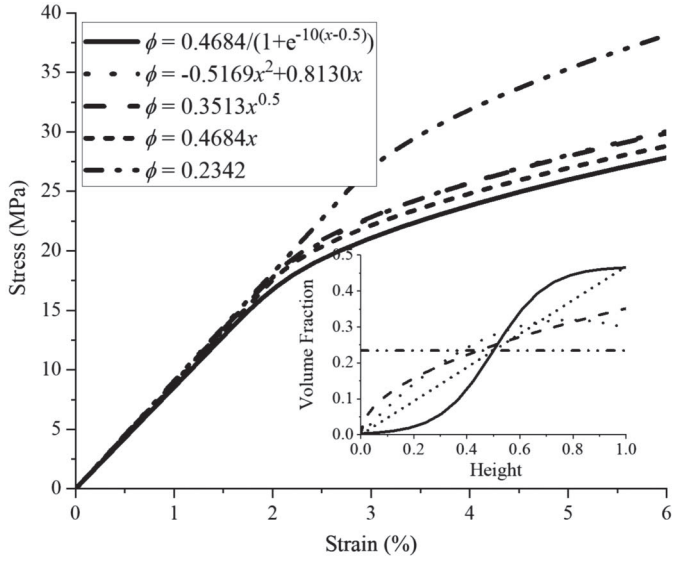


**Fig. 3.** Stress-strain curve for Al/HDPE composites with different distributed functions at the same overall particle volume fraction of 23.42%.

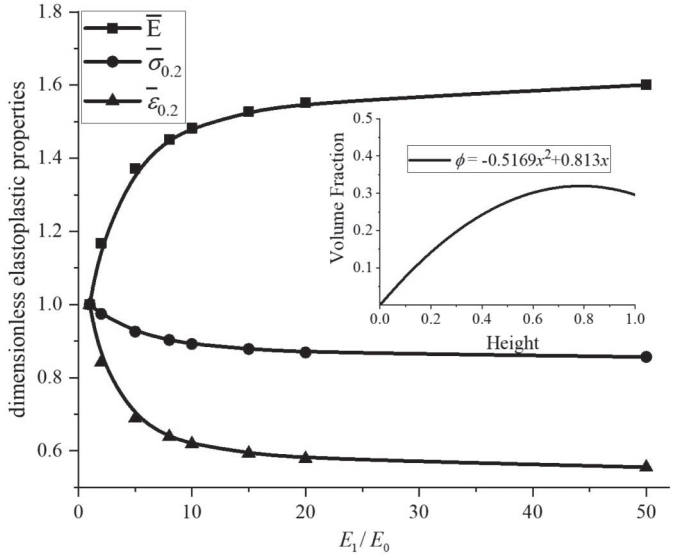


**Fig. 4.** Dimensionless overall effective elastoplastic properties shown varying with $\mathbf{E}_1/\mathbf{E}_0$, where $\mathbf{E}_1$ and $\mathbf{E}_0$ are Young's moduli of particle and matrix, respectively.

$E_e$ remained almost the same, with a variation smaller than 6%. However, the offset yield stress $\sigma_{0.2}$ showed much greater variation, up to around 37%. It was concluded that particle gradation has a small effect on elastic behavior but a large influence on plastic behavior.

Significantly, although the homogeneous mixture provided better plastic behavior, the special advantage of material gradation was jeopardized. One of the greatest advantages of FGMs is their ability to tailor particle distribution for optimal design considering both the thermal and the elastoplastic behavior of FGM panels.

### *Effect of Elastic Constant Variation*

Apart from overall volume fraction and particle distribution, particle and matrix relative stiffness has an important effect on the overall elastoplastic behavior of FGMs. Fig. 4 shows the effect of Young's modulus ratio on the dimensionless mechanical properties based on the particle volume fraction as $\phi(x) = -0.5169x^2 + 0.8130x$. Each mechanical property is divided by its corresponding value in the pure matrix stage to reach its dimensionless phases. Fig. 4 shows that the monotonically increase in particle stiffness makes a gradually weakening contribution to overall stiffness. It is seen from the plot in Fig. 4 that all of the overall effective mechanical properties grow almost linearly with the Young's modulus ratio when the ratio is smaller than 8, and gradually stabilize when the ratio is larger than 15, which means that particles with a stiffness 100 times stronger than the matrix stiffness make a similar contribution to overall stiffness, such that the particles 15 times stronger. It is interesting that the increase in particle stiffness does not guarantee a linear increase in overall effective stiffness and that its strengthening effect quickly fades when the stiffness ratio is higher than about 20. It is also straightforward to conclude that an optimal particle stiffness exists, from the elastoplastic point of view, that avoids its potential waste. Also, matrix stiffness plays an important role in overall effective stiffness and should not be neglected in elastoplastic design.

## Summary and Conclusions

A micromechanics-based algorithm to predict the elastoplastic behavior of FGM was presented. The pairwise interaction between particles was determined to account for the higher-order effect of particles on the matrix. The microscopic stress norm was transformed into the macroscopic stress norm for the yield function with ensemble average stress components. The coupling effect of neighboring layers was considered numerically, through the backward Euler's method, in calculating the relationship between ensemble average stress and far-field stress. It was determined that, when material gradation was zero, the proposed algorithm could be applied to homogeneous composites. The uniaxial elastoplastic compression tests on FGMs were conducted to validate the proposed algorithm. The elastoplastic behavior prediction based on authentic particle distribution was discussed and compared with experimental results. Despite a slight overestimation of stiffness, which may have been caused by potential defects in the samples, such as interfacial debonding and microcracking, the model well predicted

**Table 2.** Comparison of $\boldsymbol{E_e}$, $\boldsymbol{\sigma_{0.2}}$, and $\boldsymbol{\varepsilon_{0.2}}$ under different distribution functions

| Distribution function | $E_e$ (MPa) | Comparison (%) | $\sigma_{0.2}$ (MPa) | Comparison (%) | $\varepsilon_{0.2}$(%) | Comparison (%) |
|---|---|---|---|---|---|---|
| Uniform | 907.14 | 0.00 | 29.34 | 0.00 | 3.434 | 0.00 |
| Root | 895.48 | −1.28 | 21.03 | −28.32 | 2.548 | −25.80 |
| Quadratic | 892.16 | −1.65 | 20.89 | −28.78 | 2.542 | −25.98 |
| Linear | 877.54 | −3.26 | 20.34 | −30.66 | 2.518 | −26.67 |
| Sigmoid | 854.65 | −5.79 | 18.67 | −36.37 | 2.384 | −30.58 |

the elastoplastic behavior of FGMs and, it is concluded, can be used for material design and analysis.

To further study the elastoplastic behavior of FGMs, parametric studies of different particle distribution functions and relative material stiffnesses were carried out. It was observed that the particle distribution function had a small effect on FGM overall elastic behavior but a large influence on plastic behavior, and that increasing particle stiffness had a very minor strengthening effect on overall stiffness when the stiffness ratio was higher than about 20. These observations are important for laboratory research and industry manufacturing.

## Acknowledgments

This study was sponsored by the National Science Foundation (IIP 1738802) for the industry-university cooperative project with Schüco USA and CMMI (1762891) and the Air Force Office of Scientific Research (AFOSR-FA9550-14-C-0058), whose support is gratefully acknowledged. The authors appreciate Dr. Liming Li for his help in the experimental tests. The authors also appreciate the support of the Henry Mitchell Weitzner Research Fund and the Pao Research Gift, which have been and will be used in research of roofing materials for solar energy applications and technologies.

## References

Ayhan, A. O. 2007. "Stress intensity factors for three-dimensional cracks in functionally graded materials using enriched finite elements." *Int. J. Solids Struct.* 44 (25–26): 8579–8599. https://doi.org/10.1016/j.ijsolstr.2007.06.022.

Ayhan, A. O. 2009. "Three-dimensional mixed-mode stress intensity factors for cracks in functionally graded materials using enriched finite elements." *Int. J. Solids Struct.* 46 (3–4): 796–810. https://doi.org/10.1016/j.ijsolstr.2008.09.026.

Birman, V., and L. W. Byrd. 2007. "Modeling and analysis of functionally graded materials and structures." *Appl. Mech. Rev.* 60 (5): 195–216. https://doi.org/10.1115/1.2777164.

Chen, F. L., X. He, and H. M. Yin. 2016. "Manufacture and multi-physical characterization of aluminum/high-density polyethylene functionally graded materials for green energy building envelope applications." *Energy Build.* 116: 307–317. https://doi.org/10.1016/j.enbuild.2015.11.001.

Eshelby, J. D. 1957. "The determination of the elastic field of an ellipsoidal inclusion, and related problems." *Proc. R. Soc. Lond. A* 241 (1226): 376–396. https://doi.org/10.1098/rspa.1957.0133.

Eshelby, J. D. 1959. "The elastic field outside an ellipsoidal inclusion." *Proc. R. Soc. Lond. A* 252 (1271): 561–569. https://doi.org/10.1098/rspa.1959.0173.

Ganapathi, M., T. Prakash, and N. Sundararajan. 2006. "Influence of functionally graded material on buckling of skew plates under mechanical loads." *J. Eng. Mech.* 132 (8): 902–905. https://doi.org/10.1061/(ASCE)0733-9399(2006)132:8(902).

Gasik, M. M. 1998. "Micromechanical modelling of functionally graded materials." *Comput. Mater. Sci.* 13 (1–3): 42–55. https://doi.org/10.1016/S0927-0256(98)00044-5.

Ju, J. W., and T. M. Chen. 1994a. "Effective elastic moduli of two-phase composites containing randomly dispersed spherical inhomogeneities." *Acta Mech.* 103 (1–4): 123–144. https://doi.org/10.1007/BF01180222.

Ju, J. W., and T. M. Chen. 1994b. "Micromechanics and effective moduli of elastic composites containing randomly dispersed ellipsoidal inhomogeneities." *Acta Mech.* 103 (1–4): 103–121. https://doi.org/10.1007/BF01180221.

Ju, J. W., and T.-M. Chen. 1994c. "Micromechanics and effective elastoplastic behavior of two-phase metal matrix composites." *J. Eng. Mater. Technol.* 116 (3): 310–318. https://doi.org/10.1115/1.2904293.

Ju, J. W., and K. H. Tseng. 1996. "Effective elastoplastic behavior of two-phase ductile matrix composites: A micromechanical framework." *Int. J. Solids Struct.* 33 (29): 4267–4291. https://doi.org/10.1016/0020-7683(95)00266-9.

Ju, J. W., and K. H. Tseng. 1997. "Effective elastoplastic algorithms for ductile matrix composites." *J. Eng. Mech.* 123 (3): 260–266. https://doi.org/10.1061/(ASCE)0733-9399(1997)123:3(260).

Kargarnovin, M. H., M. M. Najafizadeh, and N. S. Viliani. 2007. "Vibration control of a functionally graded material plate patched with piezoelectric actuators and sensors under a constant electric charge." *Smart Mater. Struct.* 16 (4): 1252. https://doi.org/10.1088/0964-1726/16/4/037.

Kumar, V., and D. Dutta. 1998. "An approach to modeling & representation of heterogeneous objects." *J. Mech. Des.* 120 (4): 659–667. https://doi.org/10.1115/1.2829329.

Mareau, C., and S. Berbenni. 2015. "An affine formulation for the self-consistent modeling of elasto-viscoplastic heterogeneous materials based on the translated field method." *Int. J Plast.* 64: 134–150. https://doi.org/10.1016/j.ijplas.2014.08.011.

Marfia, S., and E. Sacco. 2018. "Multiscale technique for nonlinear analysis of elastoplastic and viscoplastic composites." *Composites Part B* 136: 241–253. https://doi.org/10.1016/j.compositesb.2017.10.015.

Misra, A., and P. Poorsolhjouy. 2015. "Granular micromechanics model for damage and plasticity of cementitious materials based upon thermomechanics." *Math. Mech. Solids* 1081286515576821. https://doi.org/10.1177/1081286515576821.

Misra, A., and V. Singh. 2013. "Micromechanical model for viscoelastic materials undergoing damage." *Continuum Mech. Thermodyn.* 25 (2–4): 343–358. https://doi.org/10.1007/s00161-012-0262-9.

Misra, A., and Y. Yang. 2010. "Micromechanical model for cohesive materials based upon pseudo-granular structure." *Int. J. Solids Struct.* 47 (21): 2970–2981. https://doi.org/10.1016/j.ijsolstr.2010.07.002.

Miyamoto, Y., W. A. Kaysser, B. H. Rabin, A. Kawasaki, and R. G. Ford. 2013. *Functionally graded materials: design, processing and applications*. New York: Springer.

Moschovidis, Z. A., and T. Mura. 1975. "Two-ellipsoidal inhomogeneities by the equivalent inclusion method." *J. Appl. Mech.* 42 (4): 847–852. https://doi.org/10.1115/1.3423718.

Park, K., G. H. Paulino, and J. Roesler. 2010. "Cohesive fracture model for functionally graded fiber reinforced concrete." *Cem. Concr. Res.* 40 (6): 956–965. https://doi.org/10.1016/j.cemconres.2010.02.004.

Paulino, G. H., H. M. Yin, and L. Z. Sun. 2006. "Micromechanics-based interfacial debonding model for damage of functionally graded materials with particle interactions." *Int. J. Damage Mech.* 15 (3): 267–288. https://doi.org/10.1177/1056789506060756.

Pompe, W., H. Worch, M. Epple, W. Friess, M. Gelinsky, P. Greil, U. Hempel, D. Scharnweber, and K. Schulte. 2003. "Functionally graded materials for biomedical applications." *Mater. Sci. Eng., A* 362 (1–2): 40–60. https://doi.org/10.1016/S0921-5093(03)00580-X.

Shen, H.-S. 2013. "Thermal postbuckling of shear deformable FGM cylindrical shells surrounded by an elastic medium." *J. Eng. Mech.* 139 (8): 979–991. https://doi.org/10.1061/(ASCE)EM.1943-7889.0000439.

Simo, J. C., and T. J. Hughes. 2006. *Computational inelasticity*. New York: Springer.

Sun, L. Z., and J. W. Ju. 2001. "Effective elastoplastic behavior of metal matrix composites containing randomly located aligned spheroidal inhomogeneities. Part II: applications." *Int. J. Solids Struct.* 38 (2): 203–225. https://doi.org/10.1016/S0020-7683(00)00026-3.

Sun, L. Z., and J. W. Ju. 2004. "Elastoplastic modeling of metal matrix composites containing randomly located and oriented spheroidal particles." *J. Appl. Mech.* 71 (6): 774–785. https://doi.org/10.1115/1.1794699.

Yang, J., S. M. Pickard, C. Cady, A. G. Evans, and R. Mehrabian. 1991. "The stress/strain behavior of aluminum matrix composites with discontinuous reinforcements." *Acta Metall. Mater.* 39 (8): 1863–1869. https://doi.org/10.1016/0956-7151(91)90155-T.

Yiatros, S., M. A. Wadee, and C. Völlmecke. 2012. "Modeling of interactive buckling in sandwich struts with functionally graded cores." *J. Eng. Mech.* 139 (8): 952–960. https://doi.org/10.1061/(ASCE)EM.1943-7889.0000470.

Yin, H. M., G. H. Paulino, W. G. Buttlar, and L. Z. Sun. 2008. "Effective thermal conductivity of functionally graded particulate nanocomposites

with interfacial thermal resistance." *J. Appl. Mech.* 75 (5): 051113. https://doi.org/10.1115/1.2936893.

Yin, H. M., L. Z. Sun, and G. H. Paulino. 2004. "Micromechanics-based elastic model for functionally graded materials with particle interactions." *Acta Mater.* 52 (12): 3535–3543. https://doi.org/10.1016/j.actamat.2004.04.007.

Yin, H. M., D. J. Yang, G. Kelly, and J. Garant. 2013. "Design and performance of a novel building integrated PV/thermal system for energy efficiency of buildings." *Sol. Energy* 87: 184–195. https://doi.org/10.1016/j.solener.2012.10.022.

Yin, H. M., and Y. T. Zhao. 2016. *Introduction to the micromechanics of composite materials*. Boca Raton, FL: CRC Press.